Noble gases as proxies of mean ocean temperature: sensitivity studies using a climate model of reduced complexity

Stefan P. Ritz [a,b,*], Thomas F. Stocker [a,b], Jeffrey P. Severinghaus [c]

[a] Climate and Environmental Physics, Physics Institute, University of Bern, Bern, Switzerland
[b] Oeschger Centre for Climate Change Research, University of Bern, Bern, Switzerland
[c] Scripps Institution of Oceanography, University of California, San Diego, USA

ARTICLE INFO

ABSTRACT

Past global mean ocean temperature may be reconstructed from measurements of atmospheric noble gas concentrations in ice core bubbles. Assuming conservation of noble gases in the atmosphere-ocean system, the total concentration within the ocean mostly depends on solubility which itself is temperature dependent. Therefore, the colder the ocean, the more gas can be dissolved and the less remains in the atmosphere. Here, the characteristics of this novel paleoclimatic proxy are explored by implementing krypton, xenon, argon, and N_2 into a reduced-complexity climate model. The relationship between noble gas concentrations and global mean ocean temperature is investigated and their sensitivities to changes in ocean volume, ocean salinity, sea-level pressure and geothermal heat flux are quantified. We conclude that atmospheric noble gas concentrations are suitable proxies of global mean ocean temperature. Changes in ocean volume need to be considered when reconstructing ocean temperatures from noble gases. Calibration curves are provided to translate ice-core measurements of krypton, xenon, and argon into a global mean ocean temperature change. Simulated noble gas-to-nitrogen ratios for the last glacial maximum are $\delta Kr_{atm} = -1.10‰$, $\delta Xe_{atm} = -3.25‰$, and $\delta Ar_{atm} = -0.29‰$. The uncertainty of the krypton calibration curve due to uncertainties of the ocean saturation concentrations is estimated to be $\pm 0.3\ °C$. An additional $\pm 0.3\ °C$ uncertainty must be added for the last deglaciation and up to $\pm 0.4\ °C$ for earlier transitions due to age-scale uncertainties in the sea-level reconstructions. Finally, the fingerprint of idealized Dansgaard-Oeschger events in the atmospheric krypton-to-nitrogen ratio is presented. A δKr_{atm} change of up to 0.34‰ is simulated for a 2 kyr Dansgaard-Oeschger event, and a change of up to 0.48‰ is simulated for a 4 kyr event.

© 2011 Elsevier Ltd. All rights reserved.

1. Introduction

A major focus of paleoclimate research is on the reconstruction of past air and sea temperatures. A large variety of proxies have been used to constrain these quantities on multiple timescales. Some examples of air temperature proxies are fossil pollen records (Overpeck et al., 1985), oxygen isotopes in speleothems (McDermott, 2004), or water isotopes in ice cores (Dansgaard et al., 1993; Johnsen et al., 2001; Jouzel et al., 2007). Lake and ocean temperatures can be determined by analyzing chironomids and diatoms (Battarbee, 2000), alkenones (Brassell et al., 1986; Brassell, 1993; Müller et al., 1998), the composition of membrane lipids of marine

Crenarchaeota (TEX$_{86}$) (Schouten et al., 2002, 2003), or the magnesium-to-calcium ratio of planktonic and benthic foraminiferal species (Barker et al., 2005; Elderfield et al., 2006; Bryan and Marchitto, 2008) in marine sediment cores. All the listed proxies have in common that they represent only local or regional climatic conditions and may be sensitive to complex and poorly understood biological processes. So far it has not been possible to obtain information of past changes in global-mean temperatures and hence of possible changes in the energy balance of the Earth.

Headly and Severinghaus (2007) describe a method to reconstruct past mean-ocean temperatures by measuring the krypton-to-nitrogen ratio (Kr/N$_2$) in air bubbles trapped in ice cores. The idea of the method is based on the assumption that noble gases and nitrogen exist in a closed atmosphere-ocean system and, due to their inertness, the total concentration within the ocean mostly depends on solubility which itself is temperature dependent. Within the ocean, noble gases and nitrogen are transported passively in the

same way as temperature. Although nitrogen is not completely inert, its source and sink processes are small and can be neglected in the present considerations (Gruber, 2004). The more gas is dissolved in the ocean, the less remains in the atmosphere. Past atmospheric gas concentrations are preserved in ice cores and can be measured. The xenon-to-nitrogen ratio (Xe/N_2) and the argon-to-nitrogen ratio (Ar/N_2) are also suitable for temperature reconstruction. However, routine Kr/N_2, Xe/N_2 and Ar/N_2 measurements from polar ice cores have not been published to this date.

The purpose of this paper is to assess the potential of these novel proxies and to investigate their relationship to changes in ocean temperature by quantifying their sensitivities to changes in ocean volume, ocean salinity, sea-level pressure and geothermal heat flux. Therefore, we have implemented Kr, Xe, Ar and N_2 into the Bern3D model, an intermediate complexity coupled ocean-atmosphere climate model (Müller et al., 2006; Ritz et al., 2011, Appendix A). Extensive model simulations yield a calibration curve to translate ice-core noble gas measurements into a global mean ocean temperature change and estimates of the associated uncertainties. For reasons of simplicity, the paper focuses on krypton. However, xenon and argon behave analogously to krypton. Finally, we determine the fingerprint of Dansgaard–Oeschger events in the atmospheric krypton-to-nitrogen ratio as a function of event duration.

Noble gases are proxies for global ocean temperature rather than for sea-surface temperature (SST). This shall be shortly illustrated here, because it may not be intuitively clear. Since there are no source or sink terms for noble gases, they are passively transported through the ocean in the same way as temperature. A cooler water parcel at the surface ocean takes up more noble gases because of increased solubility. As the water parcel is transported to the abyss, so are the dissolved gases. If it can be assumed that the surface ocean is always saturated with respect to the noble gases, then a direct link between temperature and the noble gases can be made because the saturation concentration is known for any given ocean temperature and salinity. A simple three-box model of the atmosphere, the surface ocean and the deep ocean illustrates that the surface ocean in fact only plays a small role, basically because of its small volume and warm temperatures compared to the deep ocean (see Appendix B for the model description). When in the model the top 100 m of the ocean warmed by 1 °C while keeping the deep ocean constant, the atmospheric Kr/N_2 ratio δKr_{atm} is increased from 0‰ to 0.014‰ (ocean salinity is kept constant at 35 psu). In contrast, when the entire ocean is warmed by 1 °C, δKr_{atm} is increased to 0.632‰.

Because ice-core measurements provide the ratio of the atmospheric krypton-to-nitrogen and the variations of this quantity are small, the delta notation is used to describe the Kr/N_2 deviations from the present-day atmosphere standard (Headly and Severinghaus, 2007):

$$\delta Kr_{atm} = \left(\frac{(Kr/N_2)_{sample}}{(Kr/N_2)_{standard}} - 1 \right) \times 1000‰. \tag{1}$$

$(Kr/N_2) = 1.46 \times 10^{-6}$ is the global and annual mean atmospheric value under modern conditions (Table 1).
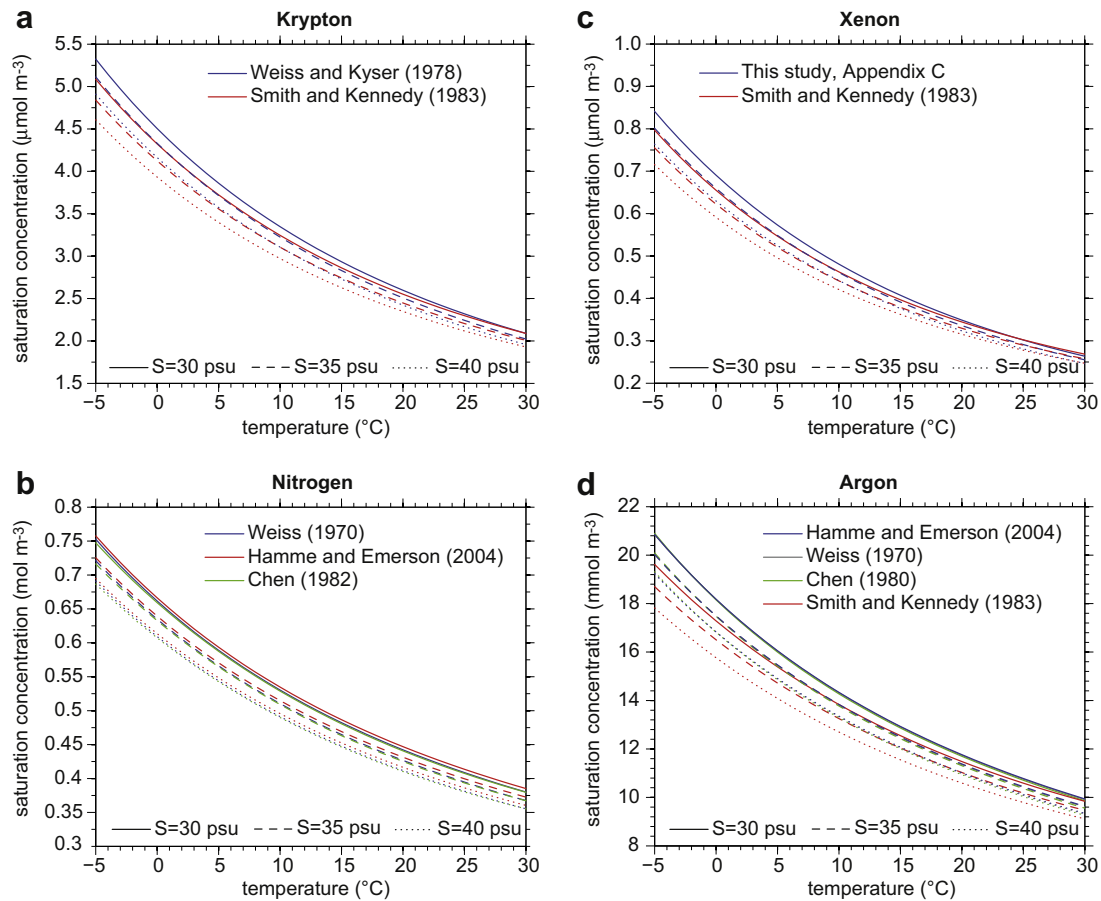
2. Model formulation of noble gases and N_2

For this study we use the Bern3D coupled ocean-atmosphere climate model (Müller et al., 2006; Ritz et al., 2011, Appendix A). It consists of a frictional geostrophic ocean model with a horizontal resolution of 36×36 grid boxes and 32 layers. The atmosphere is described by a two-dimensional energy and moisture balance model with the same horizontal resolution as the ocean. Sea ice is dynamically calculated. The noble gases and nitrogen are implemented as follows: Because of the large abundance of the gases in the atmosphere, the surface ocean is assumed to approach saturation (this assumption is tested below). The air-sea gas exchange is calculated as

$$F_{as} = k(C_s^* - C_s), \tag{2}$$

where C_s is the sea-surface concentration (mol m^{-3}), C_s^* the saturation concentration (in mol m^{-3}) and k the gas transfer velocity for seawater (in m s^{-1}, Eq. A.1) and is a function of the fractional sea-ice cover, the surface wind speed, and the Schmidt number Sc. Gas exchange is suppressed in sea-ice covered areas. Sc is taken from Wanninkhof (1992). For xenon, Sc is calculated as described by Wanninkhof (1992) using coefficients provided by Jähne et al. (1987) (see Appendix C for details). The saturation concentration of krypton is calculated from the solubility in ml air at standard temperature and pressure (STP) per kg seawater taken from Weiss and Kyser (1978), and by using 22.3511 l air/mol Kr at STP (Dymond and Smith, 1980), and the local density of seawater from the model. The saturation concentrations of argon and nitrogen in μmol kg^{-1} seawater are taken from Hamme and Emerson (2004), the saturation concentration of xenon in μmol kg^{-1} seawater is given in Appendix C. Saturation concentrations of these gases have also been reported by other studies (see Fig. 1 for an overview). Except for the saturation concentrations reported by Smith and Kennedy (1983), they differ by less than 2%. To address the uncertainty introduced by the choice of the saturation concentration, simulations are done using the saturation concentrations of Smith and Kennedy (1983) for krypton (see Appendix D and the calibration uncertainties section). The saturation concentrations depend on SST, sea-surface salinity, and sea-level pressure. The dependence on SST is nonlinear.

Apart from the air-sea fluxes (Eq. (2)), noble gases and nitrogen are assumed to be conservative within the ocean. This is not entirely true for nitrogen, because denitrification and nitrogen fixation are source and sink processes for N_2. However, they have a negligible effect on the total oceanic N_2 inventory of approximately 2×10^7 Tg N (calculated from values from Table 1), since denitrification adds only 245 ± 70 Tg N per year to the ocean whereas nitrogen fixation removes 135 ± 60 Tg N per year from the ocean (Gruber, 2004). Denitrification occurs mainly in oxygen

Table 1

Atmospheric composition, molecular weights, and mean ocean concentrations of the simulated gases compared to observations (Quinby-Hunt and Turekian, 1983; Sarmiento and Gruber, 2006; Gruber, 2008). In brackets are the values used for the relative difference. Note that the relative differences are not very accurate because of the low precision of the observations. To calculate ocean inventories, a modern ocean volume of 1.34×10^{18} m^3 determined from the ETOPO5 bathymetry data is used. The total mass of dry air is 5.119×10^{21} g (Schlesinger, 1997; Sarmiento and Gruber, 2006).

Gas	Molar weight (g mol^{-1})	Atmospheric relative composition in dry air	Mean Ocean Conc. observed (μmol m^{-3})	Mean Ocean Conc. modeled (μmol m^{-3})	Relative difference (%)
Dry air	28.9644	1	–	–	–
N_2	28.0134	0.78084	575,000	580,000	1
Ar	39.948	0.934×10^{-2}	16,000	15,700	2
Kr	83.80	1.14×10^{-6}	3.8	3.80 (3.8)	0
Xe	131.30	8.7×10^{-8}	0.5	0.58 (0.6)	20

Fig. 1. Overview of the published saturation concentrations of krypton, nitrogen, xenon, and argon. The saturation concentrations of the different studies deviate by less than 2% except for the saturation concentrations given by Smith and Kennedy (1983) that are up to 7% lower for cold temperatures. The saturation concentrations displayed are for modern sea-level pressure conditions. The dependency between the saturation concentration and temperature is nonlinear. The saturation concentration scales linearly with sea-level pressure according to Henry's law.

minimum zones in the Arabian Sea and in the eastern tropical Pacific, whereas nitrogen fixation is located to a large degree in the subtropical North Atlantic (Gruber and Sarmiento, 1997; Hansell et al., 2004). Because these regions are far from deep water formation zones, a potential regional decoupling of the dissolved nitrogen concentration from temperature is not propagated to the large volume of the abyss and is therefore insignificant.

The atmospheric inventory is calculated as described by Headly and Severinghaus (2007). The atmosphere-ocean system is assumed to be a closed system. The terrestrial biosphere reservoir, including soil organic matter, is estimated to contain only 0.002% of the total nitrogen mass (Schlesinger, 1997) and is therefore neglected. Thus, the total gas inventory of the atmosphere-ocean system

$$I_{tot}^g = I_{atm}^g + I_{ocn}^g \qquad (3)$$

is constant and does not change even for different climate states. The superscript g denotes the gas species Kr, Xe, Ar or N$_2$. I_{tot}^g can be calculated for present-day conditions because today's I_{atm}^g is known and I_{ocn}^g is calculated by the model under present-day conditions (Ritz et al., 2011). Global ocean volume is determined from 5-min gridded elevations/bathymetry data (ETOPO5; see http://www.ngdc.noaa.gov/mgg/global/etopo5.html). The present-day I_{atm}^g is calculated by multiplying the known mole fraction of the gas in the present-day atmosphere by the total amount of air in moles. The total moles of air are determined by dividing the total mass of the atmosphere by its molar weight. The values used for the calculation

are given in Table 1. Modeled mean ocean concentrations compare well with observations (Sarmiento and Gruber, 2006) as shown in Table 1. The relative differences between modeled concentrations and observations are below 5% for Kr, N$_2$ and Ar and 20% for Xe. However, because of the low precision of the observations, these values need to be taken with caution. For climate states different from present-day, I_{atm}^g is calculated as a residual, i.e. $I_{atm}^g = I_{tot}^g - I_{ocn}^g$. Changes in sea-level pressure are taken into account by scaling the saturation concentration C_s^*. According to Henry's law, the partial pressure and the dissolved concentration of a gas are directly proportional. Because the ocean component of the Bern3D model has a rigid-lid, changes in ocean volume are taken into account offline by scaling I_{ocn}^g.

To estimate the influence of bubble injection processes that would enhance air-sea gas exchange, the parameterization of Stanley et al. (2009) is implemented in our model. The parameterization considers bubbles that dissolve completely as well as bubbles that only partially dissolve. Bubble injection increases the modern ocean krypton inventory by 2% ($\pm$0.5% depending on the parameter choice) and the nitrogen inventory by 7.5% ($\pm$1%). We find that the influence of bubble injection on δKr_{atm} is negligible. In model simulations of different climate states with and without the bubble injection parameterization, δKr_{atm} differed by less than 0.04‰. Therefore, bubble injection processes are not further considered in the simulations of this paper.

To test the assumption of noble gas abundance within the atmosphere, we have also implemented into the model the

possibility of directly simulating atmospheric concentrations. Air-sea gas exchange is then calculated as

$$F_{as} = k(\beta C_a - C_s), \tag{4}$$

with C_a the atmospheric concentration (mol m^{-3}) and β the Bunsen solubility coefficient taken from Weiss and Kyser (1978) for krypton, and Weiss (1970) for nitrogen, respectively. β is defined as the volume of gas at standard temperature and pressure absorbed per unit volume of liquid. The explicit simulation of gases in the atmosphere permits the comparison of the model to present-day measurements of the seasonal cycle of δAr_{atm}. These seasonal variations have been measured at several globally distributed sites showing variations of 0.009‰–0.026‰ (Cassar et al., 2008, peak-to-peak) and 0.005‰–0.015‰ (Keeling et al., 2004), absolute differences between 3-month averages, Feb/Mar/Apr minus Aug/Sep/Oct). Seasonal variations of δAr_{atm} are simulated to be from 0.001‰ to 0.013‰ (peak-to-peak), and from 0‰ to 0.011‰ (differences between 3-month averages), respectively. In the simulation, transport in the atmosphere is parameterized by diffusion. The same diffusivities are used as for the transport of heat (Table A.1). Although not inconsistent, the model results are at the lower end of the range given by the observations. The observed seasonality in δAr_{atm} could easily be achieved by using a reduced gas-specific eddy-diffusivity in the atmosphere.

In a steady-state modern climate, this method of explicitly simulating the atmosphere leads to a 4.5% lower ocean krypton inventory and to a 5.5% lower nitrogen inventory compared to when the air-sea gas exchange formulation of Eq. (2) is used. Simulating the entire atmosphere-ocean system has the disadvantage that changes in ocean volume and sea-level pressure cannot be taken into account because of the rigid-lid formulation of the ocean model. Therefore, and because the differences between both methods are small, we use air-sea gas exchange as calculated in Eq. (2) for all simulations.

3. Sensitivity of δKr_{atm} to various model parameters

3.1. The modern ocean

To determine the dependence of δKr_{atm} on temperature and other factors, the sensitivity of δKr_{atm} to changes in atmospheric CO_2, ocean diapycnal diffusivity K_d, and wind stress is tested using our model. Changes in atmospheric CO_2 affect atmospheric temperatures and therefore ocean temperatures. CO_2 is varied within the range of 40%–200% of the pre-industrial value of 278 ppm. Every simulation is run for 20,000 years into steady state. Changes in K_d and wind stress affect mixing within the ocean which also results in an ocean temperature change. We vary K_d in a range from 10^{-8} to 10^{-4} m^2 s^{-1} (standard value: 10^{-5} m^2 s^{-1}). In the wind stress runs, wind stress is scaled by 18%–200%.

Apart from simulations with wind stress below 70% of the modern forcing, the CO_2, diapycnal diffusivity, and wind stress sensitivities show a clear relationship between global mean ocean temperature and δKr_{atm} (Figs. 2 and 3). In the model, the colder the ocean, the smaller is the sensitivity of δKr_{atm} to ocean temperature, because more extended sea-ice cover reduces air-sea gas exchange leading to surface waters which no longer saturate in Kr and N_2. To illustrate the influence of sea ice, the δKr_{atm} sensitivity simulations to CO_2 are repeated with the exception that in these simulations sea ice does not influence air-sea gas exchange. In Eq. (A.1), we set $A_i = 0$. In a third set of simulations, the sea surface is assumed to be saturated (Fig. 4). The ocean noble gas inventory becomes sensitive to sea ice when sea ice covers deep water formation areas, because then undersaturated waters are transported to the large volumes of the deep ocean. The difference between the two cases where sea ice does not play a role and where the surface ocean is saturated is minor suggesting that surface waters saturate without the presence of sea ice. The results of a two-box model (Eq. B.6) and the box model of Headly and Severinghaus (2007) agree with these simulations.

The fact that the saturation concentrations depend nonlinearly on temperature leads to the possibility that the ocean can have different gas inventories for a particular mean ocean temperature due to the spatial temperature distribution within the ocean. An ocean with a uniform temperature, for instance, would take up less gas than an ocean with a wide range of temperatures (that average to the same mean ocean temperature). The comparison of the calibration curve of the 2-box model, that consists of a uniform ocean, with the calibration curve of the Bern3D model shows that this effect is small.

Sensitivity simulations with wind stress forcing below 70% of the modern forcing show a different behavior than the rest of the simulations. In these cases the reduced wind stress substantially weakens the mixing within the ocean, especially in the Southern Ocean. For example, in the 50% wind stress case, the Drake Passage throughflow weakens from 45 Sv (1 Sv = 10^6 m^3 s^{-1}) in the standard case to 31 Sv, and the Southern Ocean overturning cell weakens from 18 Sv to 17 Sv. These circulation changes lead to colder SSTs at high latitudes in combination with an expansion of the sea-ice cover. Krypton concentrations in Southern Ocean surface waters near Antarctica drop down to 89% of the saturation concentration. In the 20% wind stress case, krypton concentrations drop down to 83% of the saturation concentration.
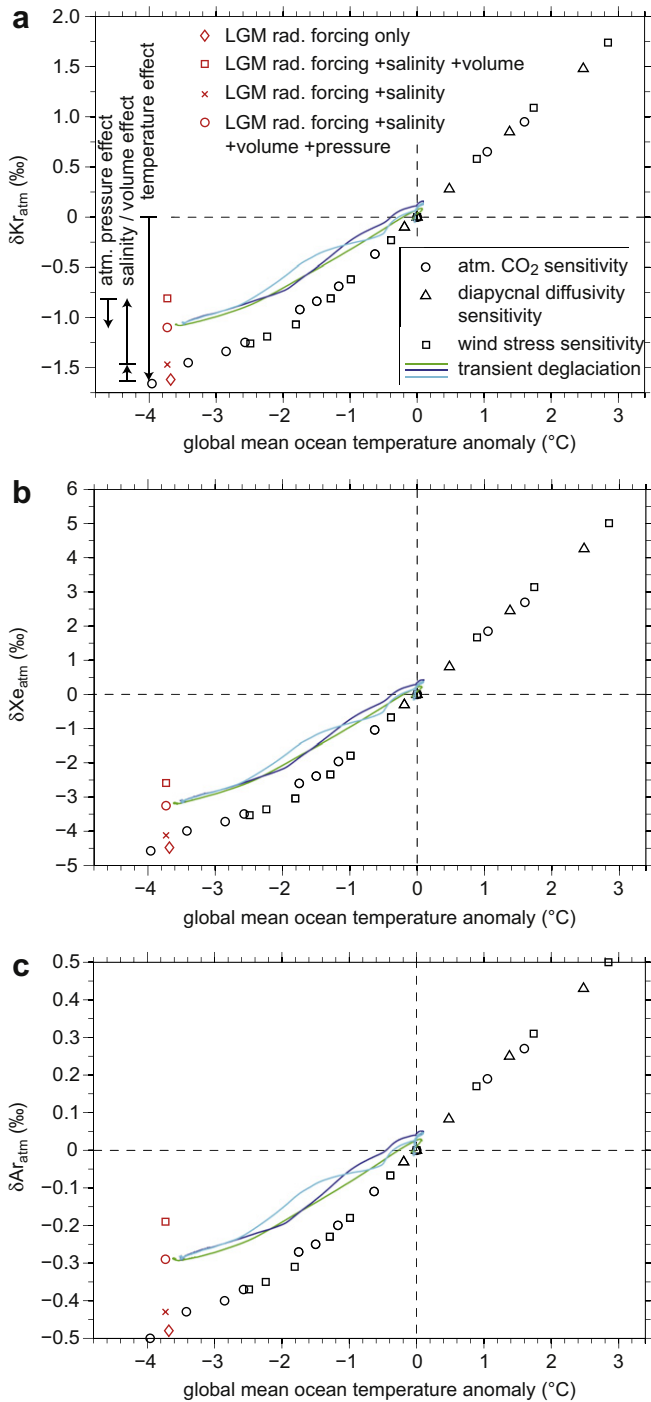
We find that sea ice decouples the noble gas concentration from the temperature signal. However, extreme situations only occur when ocean mixing is very low and the Southern Ocean is sea-ice covered to approximately 65°S throughout the year. Due to the low mixing the waters below sea ice are less quickly exchanged by saturated waters from ice-free regions. It must also be mentioned that the wind-driven gyre transport is too weak in the model (Müller et al., 2006). The modeled Drake Passage throughflow for example is with 45 Sv much weaker than the observation-based estimate of 140 Sv by Ganachaud and Wunsch (2000). Therefore, Southern Westerlies and consequently the Antarctic Circumpolar Current must face an even larger change than the model suggests to produce this extreme decoupling of δKr_{atm} from ocean temperature.

The relationship between δXe_{atm} and temperature (Fig. 2b) and δAr_{atm} and temperature (Fig. 2c) are analogous to the δKr_{atm} results. Our simulations yield a linear relationship between the noble gases for constant sea-level conditions: $\delta Xe_{atm} = 2.84 \times \delta Kr_{atm}$ ($R^2 = 0.997$) and $\delta Ar_{atm} = 0.29 \times \delta Kr_{atm}$ ($R^2 = 0.998$). Because of this very tight relationship between the different noble gases, we limit our simulations to krypton.
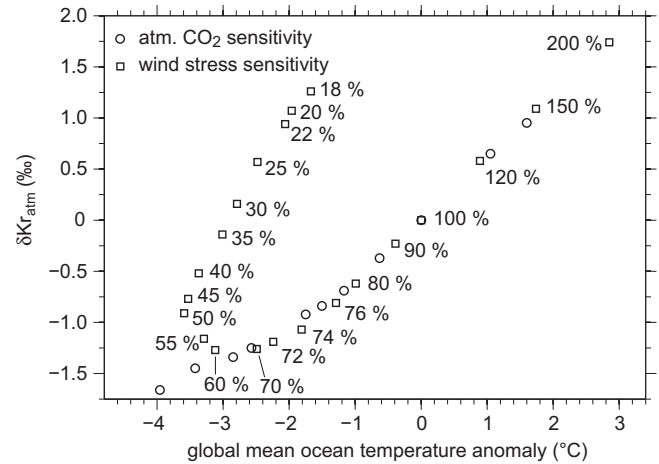
3.2. Last glacial maximum

To quantify the contribution of changes in ocean salinity, ocean volume and sea-level pressure to δKr_{atm} during glacial-interglacial cycles, several last glacial maximum (LGM) simulations are performed (Fig. 2). In these simulations we apply a set of LGM conditions and run the model for 10,000 years to steady state. In the first (referred to as LGM1), only the radiative forcing is adjusted to LGM conditions, i.e. atmospheric CO_2 is set to 180 ppm, atmospheric CH_4 to 350 ppb, and land-surface albedo is adjusted to take into account the presence of ice sheets as described in Ritz et al. (2011). Not taken into account are changes of the atmospheric dust load and changes of land albedo due to changes in vegetation and snow cover. These processes would likely lead to a further cooling of the LGM climate. The difference between modern and LGM δKr_{atm} in LGM1 is the contribution of the global mean ocean temperature change. In the

Fig. 3. Relationship between δKr_{atm} and global mean ocean temperature anomaly for simulations where the wind stress was scaled in a range from 18% to 200%. For comparison, the atmospheric CO_2 sensitivity simulations are also shown (Fig. 2a). In the simulations with wind stress below 70% of the modern value, δKr_{atm} decouples from ocean temperature because of large Southern Ocean sea-ice extent combined with low wind-driven ocean mixing.

second simulation (LGM2), additionally the change in ocean salinity is taken into account. Mean ocean salinity increases by 1.2 psu to 36.0 psu, sea-surface salinity also increases by 0.9 psu to 35.0 psu due to the ice-sheet buildup which lowers sea-level. The difference between LGM2 and LGM1 determines the contribution of the ocean salinity change on δKr_{atm}. The change in ocean salinity also invokes small circulation changes: The Atlantic meridional overturning circulation (AMOC) and the Southern Ocean overturning circulation decrease by about 2 Sv and a 1 km deep North Pacific overturning cell is established. These changes cool the global ocean by 0.05 °C and alter the temperature depth profile to slightly warmer temperatures
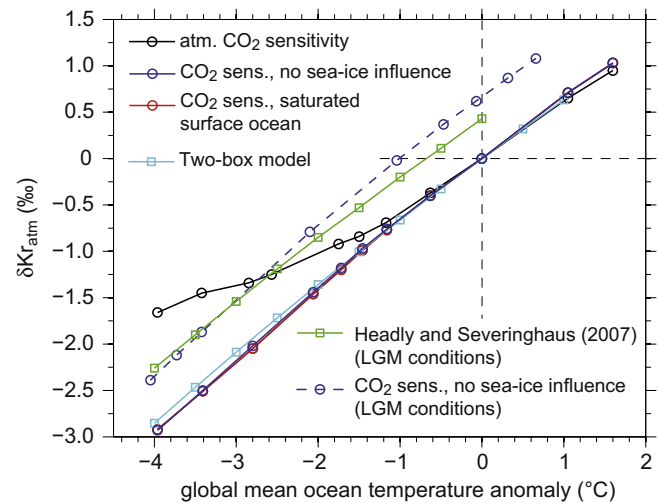

Fig. 2. Atmospheric noble gas ratio as a function of global mean ocean temperature anomaly. a) Relationship between δKr_{atm} and mean ocean temperature for various simulations. Black symbols: sensitivities of atmospheric CO_2 concentration, ocean diapycnal diffusivity, and wind stress on mean ocean temperature and δKr_{atm}. CO_2 is varied within the range of 40%–200% of the pre-industrial value of 278 ppm, diapycnal diffusivity from 10^{-8} to 10^{-4} m^2 s^{-1} (standard value: 10^{-5} m^2 s^{-1}, and wind stress is scaled by 70%–200%. The simulations show a clear relationship between δKr_{atm} and mean ocean temperature. Red symbols: δKr_{atm} and mean ocean temperature values for various LGM simulations relative to the modern steady state. The factors which control δKr_{atm} (temperature, salinity, ocean volume and sea-level pressure) are separated in the simulations to quantify each contribution (arrows). Dark and light blue lines: transient deglaciation simulation using two scenarios of the Barbados sea-level record (Peltier and Fairbanks, 2006) (see Fig. 5a). Green line: transient simulation using the benthic $\delta^{18}O$ stack ocean volume proxy of Lisiecki and Raymo (2005). Except for the transient simulations, all simulations are run into steady state. b) Analogous for δXe_{atm}. c) Analogous for δAr_{atm}.

Fig. 4. The influence of sea ice on the krypton calibration curve. Black line: the standard atmospheric CO_2 sensitivity simulations (Fig. 2a). Solid dark blue line: results of the atmospheric CO_2 sensitivity simulations when sea ice does not influence air-sea gas exchange. Red line: atmospheric CO_2 sensitivity where the surface ocean is saturated at all times. The similarity of these two curves suggests that surface waters saturate when sea ice is not present. Light blue line: results from a simple two-box model compare well with the Bern3D results (Eq. B.6). Green line: calibration curve from the box model of Headly and Severinghaus (2007). The curve is shifted relative to the other curves because their model is set to LGM conditions (i.e. LGM ocean volume, salinity, and sea-level pressure). For comparison, the CO_2 sensitivity simulations where sea ice does not influence air-sea gas exchange are repeated under LGM conditions (dashed dark blue line). The results compare well to the results of Headly and Severinghaus (2007).

in the top 1000 m and to cooler temperatures below 1500 m depth. Thus, temperature contributes indirectly to the δKr_{atm} change. A third simulation (LGM3) additionally takes into account the smaller ocean volume. Again, ocean volume is calculated from the ETOPO5 bathymetry data. Changes in the bathymetry due to the deformation of the Earth's surface by ice sheets are not taken into account. The ocean volume contribution to the δKr_{atm} change follows from the δKr_{atm} difference between LGM3 and LGM2. The presence of large ice-sheets and the lower sea-level during the last ice age also lead to an increased sea-level pressure (Mélières et al., 1991) that in turn increases saturation concentrations (Headly and Severinghaus, 2007). This effect is additionally taken into account in simulation LGM4. Using the model of Mélières et al. (1991), we calculate an LGM-to-modern sea-level pressure difference of 13.8 hPa to 14.4 hPa. We use the average (14.1 hPa). Hence, the difference between LGM4 and LGM3 determines the sea-level pressure contribution. Because ocean volume, salinity and sea-level pressure are coupled, the contributions are combined and henceforth referred to as sea-level contribution.

The temperature contribution is clearly the most important (Fig. 2a). Still, it is noteworthy that the sea-level contribution is substantial even though ocean volume itself only changes by about 3% and sea-level pressure by about 1%. The reason is that δKr_{atm} is proportional to the $I^{Kr}_{atm}/I^{N_2}_{atm}$ fraction. Although the relative change of I^{g}_{ocn} is the same for all gases g, the relative change of I^{g}_{atm} depends on the solubility of the particular gas. Nitrogen, for instance, is much less soluble than krypton. Thus, $I^{N_2}_{atm}/I^{N_2}_{ocn}$ is larger than $I^{Kr}_{atm}/I^{Kr}_{ocn}$ and hence the relative change of $I^{N_2}_{atm}$ is smaller than the change of I^{Kr}_{atm}. Therefore, in order to generate a calibration curve for the noble gas proxy, the history of sea-level change must be known and taken into account. This is of particular importance as the temperature effect and the sea-level effect point in opposite directions.

3.3. Last deglaciation

In three transient deglaciation simulations from the LGM to the present-day (Fig. 2) all the contributions discussed above are combined. In the first, the model is forced as described by Ritz et al. (2011) by atmospheric CO_2, CH_4, insolation and a simple ice-sheet/ocean volume parameterization which is tied to the Lisiecki and Raymo (2005) benthic $\delta^{18}O$ stack (LR05, Fig. 5a). High-frequency variability of LR05 was removed by applying a spline fit following Enting (1987) with a cutoff period of 10 kyr. In the other two transient deglaciation simulations, the more accurate Barbados uplift-corrected eustatic sea-level record of Peltier and Fairbanks (2006) is used. A spline with cutoff period of 1.5 kyr is applied to the sea-level data. Two different sea-level scenarios are considered due to the uncertainty of the measurements at around 13 kyr B P (before present, i.e., before 1950 A D; Fig. 5a).

The differences between the three calibration curves underlines the importance of an accurate sea-level proxy for the δKr_{atm} calibration curve. The two simulations forced by the Barbados sea-level record differ mainly by a rapid sea-level rise which takes place at about 14 kyr B P in Scenario A (Fig. 5a), and at about 11.5 kyr B P in Scenario B, respectively. The resulting calibration curves are shifted by as much as 0.3 °C. For earlier deglaciations, where sea-level records such as the Barbados record are not available, less accurate sea-level data such as the LR05 stack or the Red Sea record (Siddall et al., 2003) must be used.

4. Calibration uncertainties

4.1. Saturation concentrations

Several studies have published polynomial fits for saturation concentrations of noble gases and nitrogen (Fig. 1). The relative

uncertainties for each fitting curve are less than 0.5%. Also the results of the different studies deviate by less than 2% except for the saturation concentrations given by Smith and Kennedy (1983) that are up to 7% lower for cold temperatures. To estimate the maximum uncertainty of the calibration curve that arises from the choice of the saturation concentration, the atmospheric CO_2 sensitivity simulations are redone using the saturation concentrations of Smith and Kennedy (1983) for krypton (see Appendix D for details on the calculation of the saturation concentration). Because the different saturation concentrations for nitrogen agree well, the saturation concentration of Hamme and Emerson (2004) is used in both cases (Fig. 6). As expected, the differences are largest for cold temperatures. The maximum calibration uncertainty is derived from the possible range of mean ocean temperature for a particular δKr_{atm} value. It is estimated to be ± 0.3 °C. However, the uncertainty is considerably smaller for warmer ocean temperatures. Also, the question must be raised whether the results of Smith and Kennedy (1983) can be trusted, because they deviate notably from the other results that are in agreement among themselves.
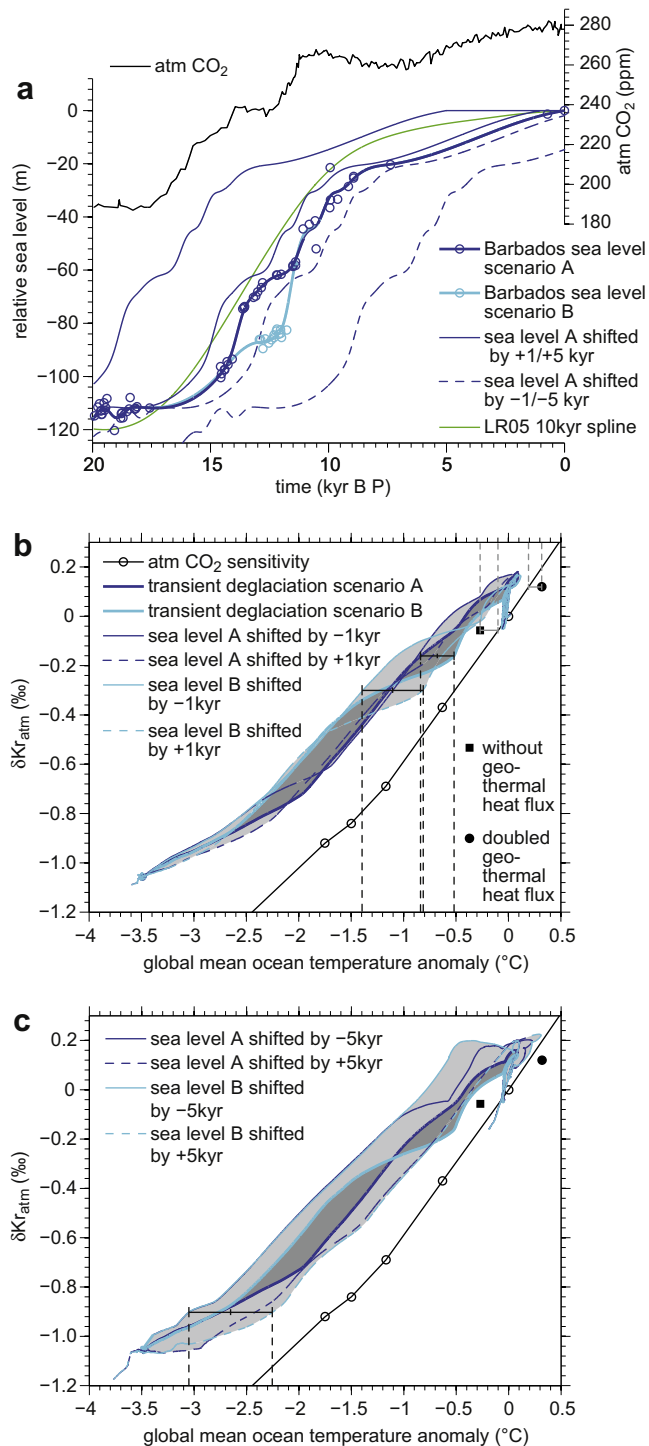
4.2. Age-scale uncertainties

As the eustatic sea levels of previous glacial and interglacial periods relative to modern are well known (approximately −120 m for the LGM, +4−6 m for the last interglacial period (Jansen et al., 2007), and references therein) but with recent studies pointing to larger values (Kopp et al., 2009)), global mean ocean temperature can be reconstructed accurately. Age-scale uncertainties become important during glaciations and deglaciations where sea-level and ocean temperatures were subject to major changes. Here, age-scales uncertainties are quantified by shifting the sea-level proxy relative to the CO_2 forcing time-series by ± 1 kyr and by ± 5 kyr in the transient simulations. Because of methane-based age-scale synchronizations between ice-cores (Blunier et al., 1998), the CO_2 record is virtually on the same age-scale as ice core δKr_{atm} measurements (the uncertainty is approximately 100 years for the last deglaciation (Blunier et al., 2007)).

During the last deglaciation, where radiocarbon dating and annual layer counting is still possible, age-scale uncertainties do not exceed 1000 yrs (Andersen et al., 2006; Rasmussen et al., 2006; Blunier et al., 2007; Reimer et al., 2009). The uncertainties of the ice core age scales arise from uncertainties in layer counting, the ice age to gas age difference, and methane synchronization. Shifting the ocean volume forcing by ± 1 kyr results in calibration curves which differ by up to 0.6 °C (thin blue lines and light gray area in Fig. 5b). The calibration curve uncertainty is therefore estimated to be ± 0.3 °C. Age-scale uncertainties are substantially larger during earlier times. Shifting the ocean volume forcing by ± 5 kyr increases the uncertainty to ± 0.4 °C (light gray area in Fig. 5c). The uncertainty of the Barbados sea-level record alone leads to a calibration curve uncertainty of ± 0.15 °C (dark gray area in Fig. 5b).

4.3. Geothermal heat flux

Geothermal heat flux contributes to the global ocean temperature. Because δKr_{atm} only records heat input at the surface ocean but the geothermal heat source is at the seafloor, the noble gas signal decouples from the temperature signal at the heat source and hence poses an additional uncertainty factor. Note that within the ocean, the gases are strongly undersaturated because of the high ambient pressure. Thus, a deep-ocean temperature increase, e.g. due to geothermal heat would not lead to outgassing. In order to estimate the uncertainty from changes in geothermal heat flux, a simulation is performed where modern geothermal heat flux is taken into account by applying the forcing field of Pollack et al.

Fig. 5. Various deglaciation forcing functions and transient simulations to determine δKr_{atm} calibration uncertainties due to age-scale uncertainties and geothermal heat flux uncertainties. a) Deglaciation forcing functions. Because ocean volume and sea-level pressure are important factors on glacial-interglacial timescales, a sea-level proxy is required for the calibration. To estimate the uncertainty due to the differences in the age-scales of the sea-level proxy and the ice-core record, the sea-level/ocean volume forcing (Peltier and Fairbanks, 2006) (thick dark and light blue lines and circles) of the transient deglaciation simulation is shifted relative to the CO_2 forcing (Monnin et al., 2001) (black line, virtually the same age-scale as the δKr_{atm} measurements) by ±1 kyr and ±5 kyr (thin blue solid and dashed lines). We distinguish two sea-level scenarios due to the uncertainty of the measurements at around 13 kyr B P. b) Relationship between δKr_{atm} and global mean ocean temperature for both sea-level scenarios without a shift (thick dark and light blue lines, as in Fig. 2) and with a shift of ±1 kyr (thin lines). The dark gray area denotes the calibration uncertainty due to the uncertainty of the sea-level record (up to ±0.15 °C). The light gray area indicates the
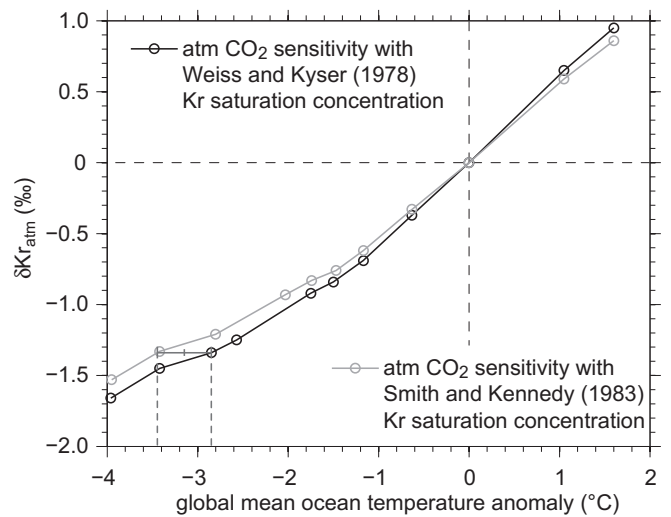
Fig. 6. Uncertainty of the krypton calibration curve due to the uncertainity of the saturation concentration. Black curve: sensitivity of δKr_{atm} to changes of atmospheric CO_2 using the saturation concentrations of Weiss and Kyser (1978) for krypton (as in Fig. 2a). Gray curve: Same sensitivity but using the saturation concentrations of Smith and Kennedy (1983) for krypton. The saturation concentrations of Hamme and Emerson (2004) are used for nitrogen in both cases because the different saturation concentrations for nitrogen agree well (Fig. 1b). The maximum calibration uncertainty is derived from the possible range of mean ocean temperature for a particular δKr_{atm} value. It is estimated to be ±0.3 °C (dashed lines).

(1993) re-gridded to the Bern3D model grid. In this case the ocean mean geothermal heat flux is 96 mW m^{-2}. In a second simulation, a doubled geothermal heat flux forcing is used. In all other simulations described in this paper, geothermal heat flux is neglected.

The global mean ocean temperature difference between zero and modern geothermal heat flux is 0.27 °C and $\delta Kr_{atm} = 0.06‰$ (Fig. 5b). The difference between doubled and modern heat flux is 0.32 °C for mean ocean temperature and $\delta Kr_{atm} = 0.12‰$. The decoupling of the noble gas signal from the temperature signal at the heat source causes a shift of the calibration curve of about 0.15 °C in both cases (Fig. 5b). Since a local temperature change at the heat source propagates to the ocean surface, the noble gases pick up a fraction of the signal. Because we consider the doubling and the shutdown of geothermal heat flux as extreme scenarios, we conclude that variations in geothermal heat flux add an uncertainty of less than ±0.15 °C.

5. Sensitivity of δKr_{atm} to ocean mixing in equilibrium and transient simulations

5.1. Equilibrium simulations

δKr_{atm} should be independent of the magnitude of ocean mixing, because krypton, N_2 and temperature are transported together in the ocean interior in a conservative fashion. To test this, a large number of model runs are performed where both the wind-stress parameter is varied from 65% to 180% of the present-day values and atmospheric CO_2 from 40% to 280% of the pre-industrial value (Fig. 7a–c). The standard diapycnal diffusivity of 10^{-5} m^2 s^{-1} is used. While wind stress changes affect mixing within the ocean as

---

uncertainty due to age-scale uncertainty during the last deglaciation (up to ±0.3 °C). Simulations without geothermal heat flux relative to modern geothermal heat flux (black square) and with doubled geothermal heat flux (black circle) shift the calibration curve by less than 0.15 °C. c) A sea level forcing shift of ±5 kyr increases the uncertainty to ±0.4 °C.

well as global ocean temperature, changes in CO_2 mainly affect ocean temperature. The result is a suite of climate states with different ocean temperatures and ocean mixing timescales, in the following expressed as AMOC strength (Fig. 7d–f). All simulations are run for 20,000 years into equilibrium.

Fig. 7d demonstrates that δKr_{atm} depends on mean ocean temperature but hardly on the AMOC strength as long as the simulations are run into equilibrium. δKr_{atm} also correlates with global mean SST (Fig. 7e) and with global mean atmospheric temperature (Fig. 7f). However, using δKr_{atm} as a proxy for SST and atmospheric temperature would additionally require information on the strength of ocean mixing. The simulations redone with a higher diapycnal diffusivity of 5×10^{-5} m^2 s^{-1} result in the same conclusions.

5.2. Dansgaard–Oeschger simulations

A suite of idealized simulations of generic Dansgaard–Oeschger events are performed in order to provide an estimate of the δKr_{atm} signal which could be expected from abrupt climate change and associated ocean temperature changes. In our simulations we consider periodic shutdowns of the AMOC of a pre-selected duration in order to investigate whether these events could be detected in the ice cores. The question is of interest because the ocean mixing timescale is an important factor on these short timescales. Ocean mixing timescales increase during weak AMOC and Southern Ocean overturning cell conditions. The experiments are separated into simulations where anomalous freshwater fluxes are applied to the North Atlantic (referred to as NA runs), the Ross Sea
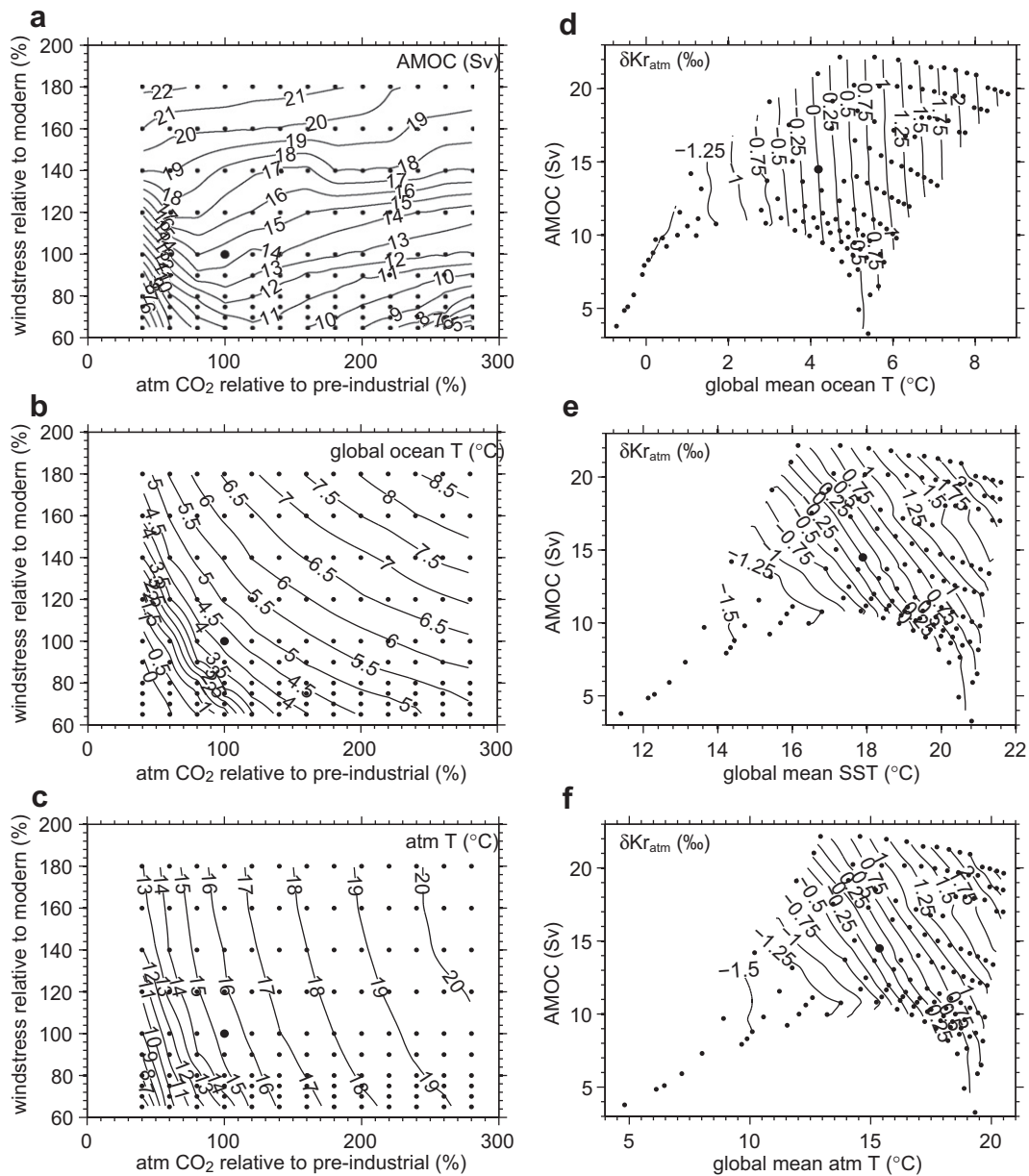
Fig. 7. Sensitivity of δKr_{atm} to ocean mixing. Every point represents a simulation of an ensemble which is run into equilibrium with a wind-stress parameter between 65% and 180% of the modern value and an atmospheric CO_2 concentration between 40% and 280% of the pre-industrial value. The reference pre-industrial steady state is represented by a larger bullet. a) AMOC strength, b) global ocean temperature, and c) atmospheric temperature of every ensemble member. d–f) δKr_{atm} as a function of the mixing timescale (expressed as AMOC strength) and mean ocean temperature, mean SST, and mean atmospheric temperature, respectively.

(RO), the Weddell Sea (WE) and both Ross and Weddell Seas (RW). In the NA case, several 24-kyr simulations are performed where the North Atlantic from 50° to 70° N is perturbed with a freshwater flux F_{FW} during τ years. The freshwater injection shuts down the AMOC. After τ years, the perturbation is reversed and freshwater is removed from the same ocean region for another τ years, whereby τ ranges from 200 to 4000 years and $F_{FW} = 0.1$ Sv. The AMOC recovers and overshoots. This periodic freshwater forcing is applied for the entire duration of the simulation.

Note that the ocean salinity change due to the freshwater perturbation has an effect on noble gas solubility. However, because the freshwater discharges associated with the Dansgaard−Oeschger events are not well known, we chose the smallest amount of freshwater required for the AMOC shutdown in order to minimize this effect. We achieve this by bringing the model close to the AMOC threshold by reducing the Atlantic-to-Pacific freshwater flux correction from 0.34 Sv (Ritz et al., 2011, Appendix A) to 0.20 Sv.

This reduces the AMOC from 14.5 Sv to 10.5 Sv at steady state. However, note that freshwater is removed from the North Atlantic during AMOC "on" phases of the simulations. This leads to an AMOC strength of approximately 17 Sv. Also note that the ocean volume change caused by the freshwater discharge is not taken into account when calculating δKr_{atm}. AMOC strength, Southern Ocean meridional overturning cell strength, mean atmospheric temperature, mean ocean temperature and δKr_{atm} time series are displayed for a section of the run in Fig. 8. Peak-to-peak values of the oscillating δKr_{atm} as a function of τ are shown in Fig. 9.

In the Southern Ocean perturbation simulations, the Atlantic-to-Pacific freshwater flux correction is not modified. Simulations are performed for the same range of τ as in the NA runs and two cases for $F_{FW} = 0.05$ and 0.1 Sv are considered. Unlike in the North Atlantic case, the freshwater perturbation is too small to shut down the Southern Ocean overturning cell completely. The overturning cell weakens from 18 Sv to approximately 14 Sv for $F_{FW} = 0.05$ Sv
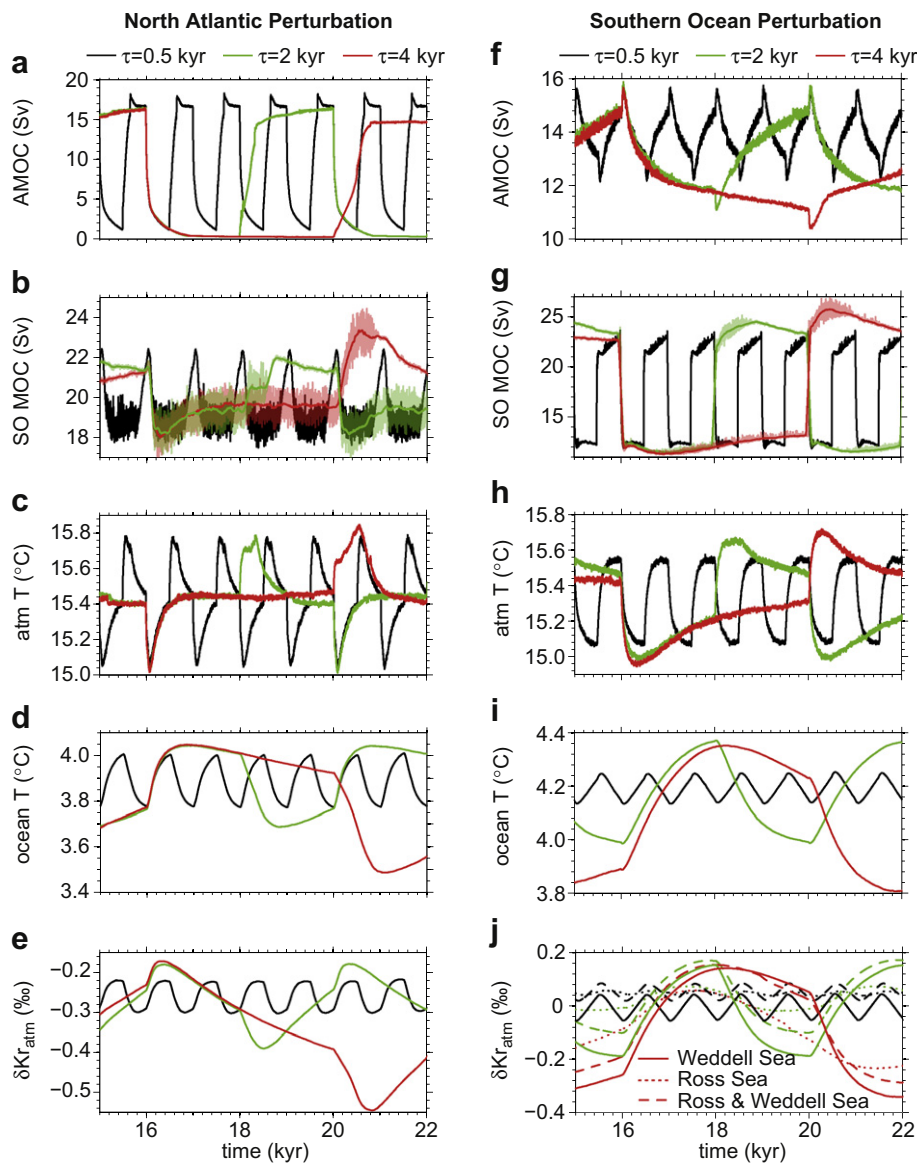
Fig. 8. The response of δKr_{atm} to idealized Dansgaard−Oeschger simulations. a−e) A section of three of the seven 24 kyr long idealized Dansgaard−Oeschger simulations NA where 0.1 Sv of freshwater is injected into the North Atlantic. f−j) Dansgaard−Oeschger simulations WE where the Weddell Sea is perturbed by 0.1 Sv of freshwater. a, f) AMOC strength. b, g) Southern Ocean meridional overturning circulation strength (absolute values). For $\tau = 2$ kyr and $\tau = 4$ kyr a 100-yr running average is calculated for better visibility. c, h) Mean atmospheric temperature. d, i) Global mean ocean temperature. e, j) δKr_{atm}. In panel j, for $\tau = 4$ kyr, δKr_{atm} of the Ross Sea perturbation (RO) and of the Ross and Weddell Sea perturbation (RW) simulation are also displayed to emphasize the similarity of the different Southern Ocean perturbation simulations.

and to approximately 12 Sv for $F_{FW} = 0.1$ Sv in all cases RO, WE and RW (Fig. 8g). The AMOC weakens gradually during the perturbation. Therefore, its strength depends on the duration of the perturbation. Again, during the recovery phases of the simulations, freshwater is removed from the ocean leading to stronger overturning cell strengths as compared to the standard values.

Fig. 9 clearly reflects an increase of the peak-to-peak δKr_{atm} change ($\Delta\delta Kr_{atm}$) with increasing perturbation duration τ. In the North Atlantic perturbation case, $\Delta\delta Kr_{atm} = 0.37$ ‰ for $\tau = 4000$ years. Note that both a stronger perturbation and taking into account the ocean volume change would increase $\Delta\delta Kr_{atm}$. A closer look at the transient evolution of NA mean ocean temperature (Fig. 8d) and δKr_{atm} (Fig. 8e) reveals slight differences. In the model, the freshwater perturbation causes a brief rise in mean ocean temperature before it drops. This rise is associated with a drop in Southern Ocean overturning cell strength (Fig. 8c), because the entire Indopacific Ocean warms when it is less fed with the cold waters of the Southern Ocean. With a short delay, the warming is overcompensated by the cooling of the entire Atlantic due to the absence of relatively warm North Atlantic Deep Water. δKr_{atm} also increases prior to the decrease. However, the drop begins earlier compared to mean ocean temperature. The origin for this decoupling lies partly with the freshening of the North Atlantic due to the freshwater discharge which increases solubility, and partly with the fact that in the model the AMOC shutdown leads to a SST reduction in the North-East Atlantic by up to 7 °C together with a sea-surface salinity reduction by around 4 psu. Both freshenings increase noble gas ocean solubility independent of temperature. The AMOC shutdown also leads to more sea ice in the North Atlantic and slightly less in the Southern Ocean, but this does not influence δKr_{atm}. Still, the temperature is the major driver of δKr_{atm}.

Comparing the North Atlantic perturbation scenarios to the Southern Ocean perturbation simulations reveals substantial differences in the behavior of global mean ocean temperature (Fig. 8d and i) and δKr_{atm} (Fig. 8e and j). In experiments RO, WE and RW, the Indopacific Ocean warms substantially due to the weakening of the Southern Ocean overturning caused by the Southern Ocean freshwater perturbation and as described above. The deep Atlantic also warms during the perturbation due to the lack of cold Antarctic Bottom Water. Because the AMOC weakens only slightly, the upper Atlantic cools only moderately. The result is a warming of the global ocean and therefore an increase of δKr_{atm}. The δKr_{atm} response to the different Southern Ocean perturbation simulations is similar but the amplitudes vary depending on the perturbation region and strength (Fig. 8j). $\Delta\delta Kr_{atm}$ values from 0.12‰ to 0.48‰ are reached for $\tau = 4000$ years (Fig. 9).

6. Conclusions

We conclude that atmospheric noble gas concentrations are suitable proxies of global mean ocean temperature. Simulated global and annual mean atmospheric noble gas-to-nitrogen ratios for the last glacial maximum are $\delta Kr_{atm} = -1.10‰$, $\delta Xe_{atm} = -3.25‰$, and $\delta Ar_{atm} = -0.29‰$. These simulated glacial-interglacial variations are ten to one hundred times larger than the seasonal variations of the present-day atmosphere. On glacial-interglacial timescales, changes in ocean volume and the associated change in sea-level pressure affect δKr_{atm} substantially, even though glacial ocean volume is only 3% smaller than during interglacial periods. Therefore, the sea-level history must be taken into account in the reconstruction. During glaciation and deglaciation periods, the timing of ocean temperature change relative to ocean volume change becomes important. Simulations of the last deglaciation using alternatively two scenarios of the Barbados uplift-corrected eustatic sea-level record of Peltier and Fairbanks (2006), and the
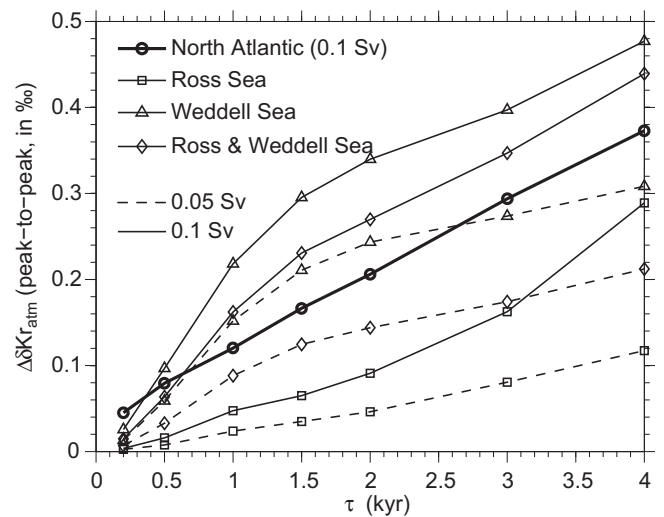

Fig. 9. Peak-to-peak amplitude of δKr_{atm} during idealized Dansgaard–Oeschger simulations as a function of freshwater perturbation duration τ (see also Fig. 8e,j) Thick line: 0.1 Sv North Atlantic perturbations (NA); squares: Ross Sea perturbations (RO); triangles: Weddell Sea perturbations (WE); diamonds: Ross and Weddell Sea perturbations (RW). For the Southern Ocean, 0.05 Sv (dashed lines) and 0.1 Sv (solid lines) perturbations are performed.

benthic $\delta^{18}O$ stack ocean volume proxy of Lisiecki and Raymo (2005) lead to an uncertainty of the calibration curve of ± 0.15 °C due to the choice of the sea-level record. Because of uncertainties in the age-scales between the ice core and the sea-level record, we estimate an uncertainty of the δKr_{atm} calibration curve of ± 0.3 °C for the last deglaciation and up to ± 0.4 °C for earlier transitions. During stadials and interstadials when sea-level was relatively constant and the values are well-established, the uncertainties are smaller. The uncertainty of the saturation concentrations adds to the calibration uncertainty. It is estimated to be ± 0.3 °C. The uncertainty which arises from geothermal heat flux changes does not exceed ± 0.15 °C. Better constraints on the krypton saturation concentrations and geothermal heat flux reduce these uncertainties.

Sea ice has the potential to decouple δKr_{atm} from ocean temperature by preventing air-sea gas exchange. However, in the model extreme decoupling only occurs when wind stress is reduced to below 70% of the modern forcing, thus under extreme climate conditions of very weak ocean mixing combined with extensive sea-ice cover in the Southern Ocean to approximately 65°S throughout the year. But because wind-driven gyre transport is too weak in the model, Southern Westerlies and consequently the Antarctic Circumpolar Current must face an even larger change than the model suggests to fully decouple δKr_{atm} from ocean temperature.

δKr_{atm} shows little dependence on the strength of ocean mixing as long as the climate is in equilibrium. Various idealized Dansgaard–Oeschger simulations provide an estimate of the δKr_{atm} signal which is produced by abrupt climate change. The resulting δKr_{atm} signal depends on the interval between subsequent abrupt changes and reaches 0.48 ‰ for a freshwater perturbation in the Weddell Sea, lasting for 4000 years, when ignoring the effect of sea-level change.

The climate model simulations presented here have implications for future measurements and their precision in order to constitute a useful paleoclimatic proxy. Together with the calibration uncertainties discussed in this paper, the precision of future ice core measurements will determine the usefulness of the noble gas proxies. The mean values and uncertainties of first results by

Headly and Severinghaus (2007) are $0.07 \pm 0.30\%_0$ and $-0.14 \pm 0.93\%_0$ for the late Holocene and $-1.34 \pm 0.37\%_0$ for the LGM. These uncertainties are high when compared with the expected signals from Dansgaard–Oeschger events simulated with this model. This suggests that measurements with significantly smaller uncertainty would be required in order to make noble gases a powerful paleoclimatic proxy for global ocean temperature changes. The simulated LGM δKr_{atm} lies within the uncertainties of the ice-core measurements. Also, the glacial-interglacial atmospheric temperature difference of 5.5 °C lies within the observation-based estimates of 4 °C–7 °C (Jansen et al., 2007). The simulated glacial-interglacial ocean temperature change, however, is in the upper range of observation-based estimates. The glacial-interglacial global annual mean SST difference for instance is estimated to be -1.9 °C ± 1.8 °C (MARGO Project Members, 2009), whereas the simulated mean SST difference is -3.5 °C. Estimates of glacial-interglacial deep ocean temperature changes based on reconstructions from Adkins et al. (2002), Waelbroeck et al., 2002), and Elderfield et al., 2010) at six distinct locations are also by 0.5 °C–2 °C lower than the model suggests. The observation-based estimates of δKr_{atm} and ocean temperature therefore suggest a higher δKr_{atm} change per degree of ocean temperature change than suggested by the model. A likely explanation for a too low model sensitivity is that the influence of sea ice on air-sea gas exchange is smaller than in the air-sea gas exchange formulation used in the model. But before such conclusions can be made, further ice-core measurements are required to confirm the first results of Headly and Severinghaus (2007).

The ability to reconstruct past global mean ocean temperature has major implications for climate research. First, the knowledge of past global mean ocean temperature gives a very valuable constraint to better tune paleoclimate models. Then, the evolution of ocean heat uptake could be constrained and with the ocean as the main storage of incoming energy (land surface and glaciers can be neglected), the evolution of the radiative imbalance of the atmosphere could be estimated.

The choice of using the cost-efficient Bern3D model for this study permitted us to perform the extensive sensitivity simulations and to run the model to equilibrium. This comes at the cost of a low spatial model resolution, however. Because the large volume of the abyssal ocean is fed by the deep water formation regions at the high latitudes, the representation of these regions in the model is important for the simulation of noble gases. Therefore, future studies should use higher grid resolution, particularly in the high latitudes. Finally, because of the rigid-lid of the ocean component of the Bern3D model, the atmospheric tracer concentrations could not be explicitly simulated under conditions when sea-level differs from the modern state, e.g., in glacial-interglacial transitions. This shortcoming should be addressed in future studies by using a free-surface ocean model.

Acknowledgments

Appendix A. Bern3D model update

The Bern3D model version used in this paper is an update to the model versions described in detail by Müller et al. (2006) and Ritz et al. (2011). An error in the radiation fluxes has been corrected and the model has been retuned. Also, the total solar irradiance has been adjusted from 1353 W m^{-2} to 1365 W m^{-2} to be in line with CMIP5 (Hurrell et al., 2011). The energy and moisture balance model parameters that have been modified are listed in Table A.1. Additionally, the following updates have been made:

Table A.1
Parameter values for the Bern3D energy and moisture transport in the atmosphere and for the sea-ice model. Parameters that have been modified with respect to the model version described by Ritz et al. (2011) are marked in bold.

Parameter	Value	Description
h_a	8194 m	atmospheric scale height for temperature
h_q	1800 m	moisture scale height
h_l	2 m	land-surface scale height
ρ_a	1.25 kg m^{-3}	reference density of air
ρ_o	1000 kg m^{-3}	reference density of water
ρ_l	2000 kg m^{-3}	reference land density
ρ_i	913 kg m^{-3}	reference density of sea ice
$c_{p,a}$	1004 J kg^{-1} K^{-1}	specific heat of air
$c_{p,l}$	1480 J kg^{-1} K^{-1}	land reference specific heat capacity
$c_{p,o}$	4044 J kg^{-1} K^{-1}	specific heat of seawater under ice
r	6.38×10^6 m	radius of the Earth
σ	5.67×10^{-8} W m^{-2} K^{-4}	Stefan–Boltzmann constant
ϵ_a	**0.8**	**atmospheric emissivity**
ϵ_o	**0.97**	**ocean emissivity**
ϵ_l	0.95	reference land emissivity (sandy, saturated soil)
S_0	**1365 W m^{-2}**	**solar constant**
τ	**5**	**cloud optical depth**
$r_{h,max}$	0.85	max. relative humidity
$r_{h,precip}$	0.7	relative humidity after precipitation
K_φ	1×10^6 m^2 s^{-1}	zonal eddy-diffusivity
K_ϑ	**$1.25 \times 10^6 + 0.5 \times \frac{\vartheta + \pi/2}{\pi}) + 1.5 \times 10^6 \cos^2\vartheta$ m^2 s^{-1}**	**meridional eddy-diffusivity**
K_φ^q	5×10^5 m^2 s^{-1}	zonal eddy-diffusivity for moisture
K_ϑ^q	5×10^5 m^2 s^{-1}	meridional eddy-diffusivity for moisture
λ	**-0.2 W m^{-2} K^{-1}**	**feedback parameter**
ΔT_{max}^{ct}	**9 °C**	**temperature reduction at cloud top when the cloud cover fraction $\xi = 1$**
K_i	10^4 m^2 s^{-1}	sea-ice diffusion coefficient
D_l	3 W m^{-2} K^{-1}	bulk coefficient for sensible heat on land
L_v	2.5×10^6 J kg^{-1}	latent heat of evaporation
L_s	2.84×10^6 J kg^{-1}	latent heat of sublimation
L_f	3.34×10^5 J kg^{-1}	latent heat of fusion of ice
c_h	0.0058	empirical constant
u_τ	0.015 m s^{-1}	skin friction velocity at ice-ocean boundary
I_{cond}	2.166 W m^{-1} K^{-1}	thermal conductivity of ice
H_0	0.01 m	minimal ice thickness
χ	0.33…0.43	continental values for fractional runoff; for Africa $\chi = 0.16$, for Antarctica $\chi = 0.83$

- In order to improve shortwave radiation through the atmosphere with respect to the data reported by Kiehl and Trenberth (1997), the parameters G_{cl} and G_{ov} of the parameterization of Bintanja (1996) (Eqs. 7 and 11 in their paper) have been increased by 12% to $G_{cl} = 0.2094$ and $G_{ov} = 0.3629$. Also, cloud optical depth τ is set to 5 and is no longer a function of surface specific humidity.
- The zonally averaged land albedo climatology of Kukla and Robinson (1980) has been replaced by zonally resolved satellite data of MODIS processed by the NASA Earth Observations (http://neo.sci.gsfc.nasa.gov).

- For sensible heat flux over land and outgoing longwave radiation the air temperatures at the corresponding altitude are used and no longer air temperatures at sea level.
- Atmospheric freshwater flux corrections have been adjusted so that the atmospheric moisture transport from the Atlantic to the Indopacific is in line with data (Zaucker and Broecker, 1992). This involves an additional freshwater flux of 0.17 Sv south of 30 N from the Atlantic to the Indopacific. The total freshwater flux correction from the Atlantic to the Indopacific is 0.34 Sv.
- The constant Ross- and Weddell Sea freshwater flux out of the ocean that stimulates convection has been increased from 0.2 Sv to 0.3 Sv. This flux correction is compensated by adding the same freshwater amount to the remaining ocean boxes around Antarctica (63°–71°S).
- The permissible range of the C_E evaporation parameter has been extended to $6.0 \times 10^{-5} \le C_E \le 1.0 \times 10^{-2}$ for better agreement between the modeled evaporation fields and ECMWF ERA-40 re-analysis data.
- Air-sea gas exchange is now a linear function of the wind speed at 10 m above ground and no longer a function of the squared wind speed as suggested by the OCMIP-2 protocol (Orr, 1999). T. Tschumi and P. Parekh (personal communication 2008) report too high modeled tracer concentrations in the Southern Ocean when using the air-sea gas transfer velocity proposed by the OCMIP-2 formulation. As a consequence, a formulation was used by Tschumi et al. (2008) and Parekh et al. (2008) where the gas transfer velocity is no longer wind-speed dependent. A more realistic formulation is now used where the air-sea gas transfer velocity is proportional to the surface wind speed:

$$k = C_1 C_2 |u| (Sc/660)^{-1/2} (1 - A_i), \tag{A.1}$$

where $C_1 = 7.798 \times 10^{-6}$ is a scaling factor to ensure that the global annual mean gas transfer velocity remains equal to the formulation of OCMIP-2, $C_2 = 0.81$ is a scaling factor proposed by Müller et al. (2008) for better agreement between modeled natural and bomb-produced ocean radiocarbon distributions and observations, $|u|$ is the cross-calibrated, multiplatform (CCMP) ocean 10 m surface wind speed climatology from the Physical Oceanography Distributed Active Archive Center (PO.DAAC, data available online at http://podaac.jpl.nasa.gov), Sc is the tracer-dependent Schmidt number, and A_i the fractional sea-ice cover.

Appendix B. Simple three-box model

Here a simple three-box model is presented that consists of an atmosphere box and a two-box ocean that is separated into a 100 m thick surface ocean layer and a deep ocean box. Ocean temperature T is the only variable changed; salinity, ocean volume, and sea-level pressure are held constant. Mass conservation requires that the total number of Kr and N_2 atoms in the ocean-atmosphere system before and after the temperature change must be equal:

$$I_a^g + I_s^g + I_d^g = I_{a,0}^g + I_{s,0}^g + I_{d,0}^g \tag{B.1}$$

The subscripts a, s, and d stand for atmosphere, surface ocean, and deep ocean, respectively. The superscript g denotes the gas species Kr or N_2, and the 0 denotes the model state before the temperature change. The inventories of each box are calculated as follows:

$$I_a^g = C_a^g V_a, \tag{B.2}$$

$$I_s^g = \beta^g(T_s) C_a^g V_s, \tag{B.3}$$

and

$$I_d^g = \beta^g(T_d) C_a^g V_d. \tag{B.4}$$

C_a^g denotes the atmospheric gas concentration, V_a, V_s, and V_d the atmospheric, surface and deep ocean volume, respectively, and β the Bunsen solubility coefficient. The deep-ocean box is in contact with the atmosphere at the deep water formation areas. β is defined as the volume of gas at standard temperature and pressure absorbed per unit volume of liquid. $V_a = 3.97 \times 10^{18}$ m^3 is calculated by multiplying the number of moles in the air (total mass of dry air times the molar weight of dry air, Table 1) by 0.02241 m^3 mol^{-1} (the volume of 1 mol gas at standard temperature and pressure). The total ocean volume is taken to be 1.34×10^{18} m^3 and is determined from the ETOPO5 bathymetry data, and $V_s = 3 \times 10^{16}$ m^3. The Bunsen solubility coefficient is taken from Weiss and Kyser (1978) for krypton, and from Weiss (1970) for nitrogen, respectively. δKr$_{atm}$ is calculated by substituting Eqs. (B.2–B.4) into Eq. (B.1) for both krypton and N_2:

$$\delta\text{Kr}_{atm} = \left(\frac{\frac{C_a^{Kr}}{C_a^{N_2}}}{\frac{C_{a,0}^{Kr}}{C_{a,0}^{N_2}}} - 1 \right) \times 1000\text{‰}$$

$$= \left(\frac{\frac{V_a + \beta^{Kr}(T_{s,0})V_s + \beta^{Kr}(T_{d,0})V_d}{V_a + \beta^{N_2}(T_{s,0})V_s + \beta^{N_2}(T_{d,0})V_d}}{\frac{V_a + \beta^{Kr}(T_s)V_s + \beta^{Kr}(T_d)V_d}{V_a + \beta^{N_2}(T_s)V_s + \beta^{N_2}(T_d)V_d}} - 1 \right) \times 1000\text{‰}. \tag{B.5}$$

As presented in the introduction, the model demonstrates that temperature changes in the surface ocean only play a small role on atmospheric δKr$_{atm}$, basically because of its small volume. The model can be simplified to a two-box model by combining the surface and deep ocean boxes to one box. In this case, $T_s = T_d$, and total volume of the ocean $V = V_s + V_d$ is used. This simplifies Eq. (B.5) to

$$\delta\text{Kr}_{atm} = \left(\frac{\frac{V_a/V + \beta^{Kr}(T_{d,0})}{V_a/V + \beta^{N_2}(T_{d,0})}}{\frac{V_a/V + \beta^{Kr}(T_d)}{V_a/V + \beta^{N_2}(T_d)}} - 1 \right) \times 1000\text{‰}. \tag{B.6}$$

The two-box model is used to calculate a calibration curve (Fig. 4). The results from the box model and from the Bern3D model are very similar when the effect of sea ice on air-sea gas exchange is not taken into account in the Bern3D model.

Appendix C. Saturation concentration and Schmidt number coefficients of xenon

Wanninkhof (1992) provides the Schmidt number of all gases discussed in this paper except xenon as a third-order polynomial fit to observations

$$Sc = A - B(T - T_0) + C(T - T_0)^2 - D(T - T_0)^3, \tag{C.1}$$

where T is the sea-surface temperature in Kelvin and $T_0 = 273.15$ K. We calculate the coefficients for xenon as described by Wanninkhof

(1992) using data of Jähne et al. (1987) and obtain the coefficients $A = 2912.9$, $B = 185.99$ K^{-1}, $C = 5.5611$ K^{-2}, and $D = 0.067645$ K^{-3}. The saturation concentration of xenon in µmol kg^{-1} seawater as a function of temperature and salinity is fitted to the data of Wood and Caputi (1966) using the polynomial

$$C_s^* = 0.98 \mu \text{mol kg}^{-1} \times \exp\left(A_0 + A_1 T_s + A_2 T_s^2 + S(B_0 + B_1 T_s)\right),$$
(C.2)

where S is the salinity in psu,

$$T_s = \log\left(\frac{298.15K + T_0 - T}{T}\right),$$
(C.3)

and the coefficients $A_0 = -7.48588$, $A_1 = 5.08763$, $A_2 = 4.22078$, $B_0 = -8.17791 \times 10^{-3}$ psu^{-1}, and $B_1 = -1.20172 \times 10^{-2}$ psu^{-1} (Hamme and Severinghaus, 2007).

Appendix D. Saturation concentrations of Smith and Kennedy (1983)

The saturation concentrations of Smith and Kennedy (1983) are given as mole fraction solubilities

$$X_g = \frac{n_g}{n_g + n_{\text{H}_2\text{O}} + n_{\text{Na}} + n_{\text{Cl}}} \approx \frac{n_g}{n_{\text{H}_2\text{O}} + n_{\text{Na}} + n_{\text{Cl}}},$$
(D.1)

where n is the number of moles of H$_2$O, Na, Cl, or of gas g, where g is either Kr, Xe, or Ar. The mole fraction solubility is converted to a saturation concentration in mol m^{-3} by converting the number of moles of the solution to grams (H$_2$O: 18 g mol^{-1}, NaCl: 58.5 g mol^{-1}) and to m^3 using the sea-surface density of the model.

The formulation of Smith and Kennedy (1983) additionally requires the NaCl molarity (mol NaCl/l water). The salinity of the model is converted from psu to molarity by assuming that 1 psu = 1 g salt/kg water. The conversion can then be done using molar weight of NaCl of 58.5 g mol^{-1}.

References

Adkins, J.F., McIntyre, K., Schrag, D.P., 2002. The salinity, temperature, and δ¹⁸O of the glacial deep ocean. Science 298, 1769–1773.

Andersen, K.K., Svensson, A., Johnsen, S.J., Rasmussen, S.O., Bigler, M., Röthlisberger, R., Ruth, U., Siggaard-Andersen, M.-L., Steffensen, J.P., Dahl-Jensen, D., Vinther, B.M., Clausen, H.B., 2006. The Greenland ice core chronology 2005, 15–42 ka. Part 1: constructing the time scale. Quaternary Science Reviews 25, 3246–3257.

Barker, S., Cacho, I., Benway, H., Tachikawa, K., 2005. Planktonic foraminiferal Mg/Ca as a proxy for past oceanic temperatures: a methodological overview and data compilation for the Last Glacial Maximum. Quaternary Science Reviews 24, 821–834.

Battarbee, R.W., 2000. Palaeolimnological approaches to climate change, with special regard to the biological record. Quaternary Science Reviews 19 (1–5), 107–124.

Bintanja, R., 1996. The parameterization of shortwave and longwave radiative fluxes for use in zonally averaged climate models. Journal of Climate 9, 439–454.

Blunier, T., Chappellaz, J., Schwander, J., Dällenbach, A., Stauffer, B., Stocker, T.F., Raynaud, D., Jouzel, J., Clausen, H., Hammer, C., Johnsen, S., 1998. Asynchrony of Antarctic and Greenland climate change during the last glacial period. Nature 394, 739–743.

Blunier, T., Spahni, R., Barnola, J.-M., Chappellaz, J., Loulergue, L., Schwander, J., 2007. Synchronization of ice core records via atmospheric gases. Climate of the Past 3, 325–330.

Brassell, S.C., 1993. Applications of biomarkers for delineating marine paleoclimatic fluctuations during the Pleistocene. In: Engel, M.H., Macko, S.A. (Eds.), Organic Geochemistry: Principles and Applications. Plenum Press, pp. 699–738.

Brassell, S.C., Eglinton, G., Marlowe, I.T., Pflaumann, U., Sarnthein, M., 1986. Molecular stratigraphy — a new tool for climatic assessment. Nature 320, 129–133.

Bryan, S.P., Marchitto, T.M., 2008. Mg/Ca-temperature proxy in benthic forami-nifera: new calibrations from the Florida Straits and a hypothesis regarding Mg/Li. Paleoceanography 23, PA2220.

Cassar, N., McKinley, G.A., Bender, M.L., Mika, R., Battle, M., 2008. An improved comparison of atmospheric Ar/N₂ time series and paired ocean-atmosphere model predictions. Journal of Geophysical Research 113, D21122.

Chen, C.-T.A., 1980. Seawater. In: Clever, H.L. (Ed.), Argon, IUPAC Solubility Data Series, vol. 4. Pergamon Press, pp. 27–32.

Chen, C.-T.A., 1982. Seawater. In: Battino, R. (Ed.), Nitrogen and Air, IUPAC Solubility Data Series, vol. 10. Pergamon Press, pp. 31–33.

Dansgaard, W., Johnsen, S.J., Clausen, H.B., Dahl-Jensen, D., Gundestrup, N.S., Hammer, C.U., Hvidberg, C.S., Steffensen, J.P., Sveinbjörnsdottir, A.E., Jouzel, J., Bond, G., 1993. Evidence for general instability of past climate from a 250-kyr ice-core record. Nature 364, 218–220.

Dymond, J.H., Smith, E.B., 1980. The Virial Coefficients of Pure Gases and Mixtures: A Critical Compilation. Clarendon Press, Oxford.

Elderfield, H., Greaves, M., Barker, S., Hall, I.R., Tripati, A., Ferretti, P., Crowhurst, S., Booth, L., Daunt, C., 2010. A record of bottom water temper-ature and seawater δ¹⁸O for the Southern Ocean over the past 440 kyr based on Mg/Ca of benthic foraminiferal Uvigerina spp. Quaternary Science Reviews 29, 160–169.

Elderfield, H., Yu, J., Anand, P., Kiefer, T., Nyland, B., 2006. Calibrations for benthic foraminiferal Mg/Ca paleothermometry and the carbonate ion hypothesis. Earth and Planetary Science Letters 250, 633–649.

Enting, I.G., 1987. On the use of smoothing splines to filter CO₂ data. Journal of Geophysical Research 92, 10,977–10,984.

Ganachaud, A., Wunsch, C., 2000. Improved estimates of global ocean circulation, heat transport and mixing from hydrographic data. Nature 408, 452–457.

Gruber, N., 2004. The dynamics of the marine nitrogen cycle and its influence on atmospheric CO₂. In: Follows, M., Oguz, T. (Eds.), The Ocean Carbon Cycle and Climate. NATO ASI Series. Kluwer Academic, Dordrecht, The Netherlands, pp. 97–148.

Gruber, N., 2008. The marine nitrogen cycle: overview and challenges. In: Capone, D.G., Bronk, D.A., Mulholland, M.R., Carpenter, E.J. (Eds.), Nitrogen in the Marine Environment, second ed. Academic Press, Amsterdam, The Neth-erlands, pp. 1–50.

Gruber, N., Sarmiento, J.L., 1997. Global patterns of marine nitrogen fixation and denitrification. Global Biogeochemical Cycles 11, 235–266.

Hamme, R.C., Emerson, S.R., 2004. The solubility of neon, nitrogen and argon in distilled water and seawater. Deep-Sea Research Part 1 (51), 1517–1528.

Hamme, R.C., Severinghaus, J.P., 2007. Trace gas disequilibria during deep-water formation. Deep-Sea Research Part 1 (54), 939–950.

Hansell, D.A., Bates, N.R., Olson, D.B., 2004. Excess nitrate and nitrogen fixation in the North Atlantic Ocean. Marine Chemistry 84, 243–265.

Headly, M.A., Severinghaus, J.P., 2007. A method to measure Kr/N₂ ratios in air bubbles trapped in ice cores and its application to reconstructing past mean ocean temperature. Journal of Geophysical Research 112, D19105.

Hurrell, J., Visbeck, M., Pirani, P., 2011. WCRP coupled model intercomparison project — phase 5-CMIP5. CLIVAR Exchanges 16 (56).

Jähne, B., Heinz, G., Dietrich, W., 1987. Measurement of the diffusion coefficients of sparingly soluble gases in water. Journal of Geophysical Research 92, 10767–10776.

Jansen, E., Overpeck, J., Briffa, K.R., Duplessy, J.-C., Joos, F., Masson-Delmotte, V., Olago, D., Otto-Bliesner, B., Peltier, W.R., Rahmstorf, S., Ramesh, R., Raynaud, D., Rind, D., Solomina, O., Villalba, R., Zhang, D., 2007. Palaeoclimate. In: Solomon, S., Qin, D., Manning, M., Chen, Z., Marquis, M., Averyt, K.B., Tignor, M., Miller, H.L. (Eds.), Climate Change 2007: The Physical Science Basis. Working Group I Contribution to the Fourth Assessment Report of the Inter-governmental Panel on Climate Change. Cambridge University Press, pp. 433–497.

Johnsen, S.J., Dahl-Jensen, D., Gundestrup, N., Steffensen, J.P., Clausen, H.B., Miller, H., Masson-Delmotte, V., Sveinbjornsdottir, A.E., White, J., 2001. Oxygen isotope and palaeotemperature records from six Greenland ice-core stations: Camp Century, Dye-3, GRIP, GISP2, Renland and NorthGRIP. Journal of Quater-nary Science 16 (4), 299–307.

Jouzel, J., Masson-Delmotte, V., Cattani, O., Dreyfus, G., Falourd, S., Hoffmann, G., Minster, B., Nouet, J., Barnola, J.M., Chappellaz, J., Fischer, H., Gallet, J.C., Johnsen, S., Leuenberger, M., Loulergue, L., Luethi, D., Oerter, H., Parrenin, F., Raisbeck, G., Raynaud, D., Schilt, A., Schwander, J., Selmo, E., Souchez, R., Spahni, R., Stauffer, B., Steffensen, J.P., Stenni, B., Stocker, T.F., Tison, J.-L., Werner, M., Wolff, E., 2007. Orbital and millennial Antarctic climate variability over the past 800,000 years. Science 317, 793–796.

Keeling, R.F., Blaine, T., Paplawsky, B., Katz, L., Atwood, C., Brockwell, T., 2004. Measurement of changes in atmospheric Ar/N₂ ratio using a rapid-switching, single-capillary mass spectrometer system. Tellus B 56, 322–338.

Kiehl, J.T., Trenberth, K.E., 1997. Earth's annual global mean energy budget. Bulletin of the American Meteorological Society 78, 197–208.

Kopp, R.E., Simons, F.J., Mitrovica, J.X., Maloof, A.C., Oppenheimer, M., 2009. Prob-abilistic assessment of sea level during the last interglacial stage. Nature 462, 863–867.

Kukla, G., Robinson, D., 1980. Annual cycle of surface albedo. Monthly Weather Review 108, 56–68.

Lisiecki, L.E., Raymo, M.E., 2005. A Pliocene-Pleistocene stack of 57 globally distributed benthic δ¹⁸O records. Paleoceanography 20, PA1003.

MARGO Project Members, 2009. Constraints on the magnitude and patterns of ocean cooling at the Last Glacial Maximum. Nature Geoscience 2, 127–132.

McDermott, F., 2004. Palaeo-climate reconstruction from stable isotope variations in speleothems: a review. Quaternary Science Reviews 23, 901–918.

Mélières, M.-A., Martinerie, P., Raynaud, D., Lliboutry, L., 1991. Glacial-interglacial mean sea level pressure change due to sea level, ice sheet and atmospheric mass changes. Global and Planetary Change 3, 333–340.

Monnin, E., Indermühle, A., Dällenbach, E., Flückiger, J., Stauffer, B., Stocker, T.F., Raynaud, D., Barnola, J.-M., 2001. Atmospheric CO2 concentrations over the last glacial termination. Science 291, 112–114.

Müller, P.J., Kirst, G., Ruhland, G., von Storch, I., Rosell-Melé, A., 1998. Calibration of the alkenone paleotemperature index U based on core-tops from the eastern South Atlantic and the global ocean (60°N-60°S). Geochimica et Cosmochimica Acta 62 (10), 1757–1772.

Müller, S.A., Joos, F., Edwards, N.R., Stocker, T.F., 2006. Water mass distribution and ventilation time scales in a cost-efficient, three-dimensional ocean model. Journal of Climate 19, 5479–5499.

Müller, S.A., Joos, F., Edwards, N.R., Stocker, T.F., 2008. Modeled natural and excess radiocarbon: sensitivities to the gas exchange formulation and ocean transport strength. Global Biogeochemical Cycles 22, GB3011.

Orr, J.C., 1999. On ocean carbon-cycle model comparison. Tellus 51B, 509–510.

Overpeck, J.T., Webb, T., Prentice, I.C., 1985. Quantitative interpretation of fossil pollen spectra: dissimilarity coefficients and the method of modern analogs. Quaternary Research 23, 87–108.

Parekh, P., Joos, F., Müller, S.A., 2008. A modeling assessment of the interplay between aeolian iron fluxes and iron-binding ligands in controlling carbon dioxide fluctuations during Antarctic warm events. Paleoceanography 23, PA4202.

Peltier, W.R., Fairbanks, R.G., 2006. Global glacial ice volume and Last Glacial Maximum duration from an extended Barbados sea level record. Quaternary Science Reviews 25, 3322–3337.

Pollack, H.N., Hurter, S.J., Johnson, J.R., 1993. Heat flow from the Earth's interior: analysis of the global data set. Reviews of Geophysics 31, 267–280.

Quinby-Hunt, M.S., Turekian, K.K., 1983. Distribution of elements in sea water. EOS 64, 130–132.

Rasmussen, S.O., Andersen, K.K., Svensson, A.M., Steffensen, J.P., Vinther, B.M., Clausen, H.B., Siggaard-Andersen, M.L., Johnsen, S.J., Larsen, L.B., Dahl-Jensen, D., Bigler, M., Röthlisberger, R., Fischer, H., Goto-Azuma, K., Hansson, M.E., Ruth, U., 2006. A new Greenland ice core chronology for the last glacial termination. Journal of Geophysical Research 111, D6.

Reimer, P.J., Baillie, M.G.L., Bard, E., Bayliss, A., Beck, J.W., Blackwell, P.G., Ramsey, C.B., Buck, C.E., Burr, G.S., Edwards, R.L., Friedrich, M., Grootes, P.M., Guilderson, T.P., Hajdas, I., Heaton, T.J., Hogg, A.G., Hughen, K.A., Kaiser, K.F., Kromer, B., McCormac, F.G., Manning, S.W., Reimer, R.W., Richards, D.A., Southon, J.R., Talamo, S., Turney, C.S.M., van der Plicht, J., Weyhenmeyer, C.E., 2009. INTCAL09 AND MARINE09 radiocarbon age calibration curves, 0–50,000 years Cal BP. Radiocarbon 51, 1111–1150.

Ritz, S.P., Stocker, T.F., Joos, F., 2011. A coupled dynamical ocean - energy balance atmosphere model for paleoclimate studies. Journal of Climate 24, 349–375.

Sarmiento, J.L., Gruber, N., 2006. Ocean Biogeochemical Dynamics. Princeton University Press, Princeton and Oxford.

Schlesinger, W.H., 1997. Biogeochemistry, an Analysis of Global Change, second ed. Academic Press.

Schouten, S., Hopmans, E.C., Forster, A., van Breugel, Y., Kuypers, M.M.M., Damste, J.S.S., 2003. Extremely high sea-surface temperatures at low latitudes during the middle Cretaceous as revealed by archaeal membrane lipids. Geology 31 (12), 1069–1072.

Schouten, S., Hopmans, E.C., Schefuss, E., Damste, J.S.S., 2002. Distributional variations in marine crenarchaeotal membrane lipids: a new tool for reconstructing ancient sea water temperatures? Earth and Planetary Science Letters 204, 265–274.

Siddall, M., Rohling, E.J., Almogi-Labin, A., Hemleben, C., Meischner, D., Schmelzer, I., Smeed, D.A., 2003. Sea-level fluctuations during the last glacial cycle. Nature 423, 853–858.

Smith, S.P., Kennedy, B.M., 1983. The solubility of noble gases in water and in NaCl brine. Geochimica et Cosmochimica Acta 47, 503–515.

Stanley, R.H.R., Jenkins, W.J., Lott III, D.E., Doney, S.C., 2009. Noble gas constraints on air-sea gas exchange and bubble fluxes. Journal of Geophysical Research 114, C11020.

Tschumi, T., Joos, F., Parekh, P., 2008. How important are Southern Hemisphere wind changes for low glacial carbon dioxide? A model study. Paleoceanography 23, PA4208.

Waelbroeck, C., Labeyrie, L., Michel, E., Duplessy, J.C., McManus, J.F., Lambeck, K., Balbon, E., Labracherie, M., 2002. Sea-level and deep water temperature changes derived from benthic foraminifera isotopic records. Quaternary Science Reviews 21, 295–305.

Wanninkhof, R., 1992. Relationship between wind speed and gas exchange over the ocean. Journal of Geophysical Research 97, 7373–7382.

Weiss, R.F., 1970. The solubility of nitrogen, oxygen and argon in water and seawater. Deep-Sea Research 17, 721–735.

Weiss, R.F., Kyser, T.K., 1978. Solubility of krypton in water and seawater. Journal of Chemical and Engineering Data 23, 69–72.

Wood, D., Caputi, R., 1966. Solubilities of Kr and Xe in Fresh and Sea Water. Tech. rep., U.S. Naval Radiological Defense Laboratory, San Francisco, CA.

Zaucker, F., Broecker, W.S., 1992. The influence of atmospheric moisture transport on the fresh water balance of the Atlantic Drainage Basin: general circulation model simulations and observations. Journal of Geophysical Research 97, 2765–2773.